LAWRENCE
LIVERMORE
NATIONAL
LABORATORY

UCRL-CONF-222438

Measurement and ALE3D Simulation of Violence in a Deflagration Experiment With LX-10 and Aermet-100 Alloy

J. Knap, M. A. McClelland, J. L. Maienschein, W. M. Howard, A. L. Nichols, M. R. deHaven, O. T. Strand

June 27, 2006

13th International Detonation Symposium
Norfolk, VA, United States
July 23, 2006 through July 28, 2006

MEASUREMENT AND ALE3D SIMULATION OF VIOLENCE IN A DEFLAGRATION EXPERIMENT WITH LX-10 AND AERMET-100 ALLOY

J. Knap, M. A. McClelland, J. L. Maienschein,
W. M. Howard, A. L. Nichols, M. R. deHaven, and O. T. Strand

Lawrence Livermore National Laboratory
Livermore, CA 94551

Abstract. We describe the results of a Scaled-Thermal-Explosion-eXperiment (STEX) for LX-10 (94.7 % HMX, 5.3 % Viton A) confined in an AerMet 100 (iron-cobalt-nickel alloy) tube with reinforced end caps. The experimental measurements are compared with predictions of an Arbitrary-Lagrangian-Eulerian (ALE3D) computer model. ALE3D is a three-dimensional multi-physics computer code capable of solving coupled equations describing thermal, mechanical and chemical behavior of materials. In particular, we focus on the processes linked to fracture and fragmentation of the AerMet tube driven by the LX-10 deflagration.

INTRODUCTION

The issue of cookoff violence is of interest in the DoD and DOE communities. In a climate of tighter restrictions concerning safety and the protection of the environment, there is a growing interest in using simulation tools to help answer questions related to fire hazards. There are both national and international efforts aimed at the reduction of hazards risks in weapons systems. There is interest in the cookoff violence behavior of explosives and propellants in current and planned missile systems. There is also the need to develop sub-scale fire tests with accompanying computer models to help rocket motor designers more effectively evaluate design options before more costly full-scale cookoff tests are performed. In addition, the Navy is interested in the design of shipboard storage facilities for munitions and developing strategies for firefighting. Finally, high power laser systems are being developed to destroy missile targets and land mines by cookoff of the contained explosives.

The goal of our effort has been advancement of predictive computer simulation capability for the violence of thermal explosions in slow and fast cookoff of energetic materials systems. The development of these computational models requires full understanding of the coupled thermal-chemical-mechanical behavior of energetic material systems exposed to thermal stimuli. In addition, it is necessary to construct computational tools to solve the associated modeling equations for the prediction of violence. In order to develop and refine our models, experimental thermal explosion tests are needed that span a spectrum of explosives, case materials, and violence results. Currently, the time to explosion for a specific time-temperature profile can be predicted for many systems, but reliable prediction of violence remains to be demonstrated. In order to properly assess the hazards from an event involving heating, prediction of the violence of thermal response is necessary.

We consider the LX-10 explosive with a nominal composition of 94.7 % HMX and 5.3 % of Viton A binder.

In this article, we present the experimental results of a STEX test for LX-10 confined in an AerMet 100 (iron-cobalt-nickel alloy) tube with reinforced end caps. However, in stark contrast with earlier studies [1], the explosion of LX-10 was induced via an igniter at room temperature, instead of externally applied thermal loading. Throughout the explosion, the tube expansion and fragment velocities were recorded, and enable us to produce a curve describing over 15 cm of tube wall motion.

We also describe a numerical model of the LX-10 STEX test. The model is based on the Arbitrary-Lagrangian-Eulerian (ALE3D) computer simulation code developed at LLNL. We give a detailed description of our numerical approach including the development of material models for both the explosive and the tube material. The model predictions are then contrasted with the experimental measurements.

SCALED THERMAL EXPLOSION EXPERIMENT

We have adopted the Scaled-Thermal-Explosion-Experiment (STEX) as a convenient basis for quantifying the violence of thermal explosions under carefully controlled conditions [1]. In this test, a thin-walled vessel (tube) with heavily reinforced end flanges is filled with a high-explosive material. The explosive charge is subsequently ignited in the central region of the cylinder, resulting in a rise of the internal pressure, ultimately leading to failure and fragmentation of the vessel. The time evolution of the tube expansion in the course of the explosion allows for accurate and quantitative characterization of the explosion violence. By virtue of its design, this experiment focuses on deflagration and fragmentation phenomena, removing all of the complexities related to chemical decomposition, thermal damage, dynamic gaps, gas flow through porous HE.

Experimental setup for STEX

The STEX employed an AerMet® 100 (iron-cobalt-nickel alloy) cylindrical tube. The internal diameter of the tube was 4.493 cm, the length 20.32 cm and the wall thickness 0.293 cm. The tube was heat-treated to give it Rockwell C hardness of 55.

The LX-10 was pressed and then machined into five cylinders 4.493 cm in diameter, a combined length of 20.32 cm, and density of 1.86 g/cm^3. In order to simplify assembly, the HE was cooled, and, subsequently, inserted cold into the tube. No detectable gap was observed between LX-10 and the inside tube wall. Two steel spacers were used to eliminate end gaps.

The explosive was ignited by means of a $BKNO_3$ igniter with imbedded HNS pellets located on the tube axis in the axial mid-plane (Figure 1).

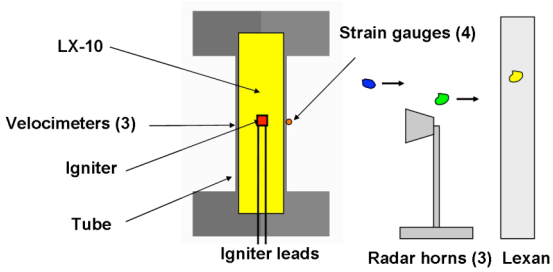

Figure 1. Schematic of the experimental setup.

The violence of the explosion was characterized by i) capture and measurement of tube fragments and ii) direct measurement of the wall velocity. The tube fragments were captured in Lexan panels located on the four sides and ceiling of the shrapnel catcher. The velocity measurements were carried out by means of a combined system that included: strain gauges, Photonic-Doppler-Velocimeter (PDV) probes, and micro-power radar systems. Two hoop (SG1 and SG2) strain gauges with maximum ranges of 8 and 2%, respectively, were measured the deformation of the tube near the axial mid-plane during the entire thermal ramp and subsequent explosion. Three PDV probes, spaced at 120°, were used to determine the wall motion of the tube at the axial mid-plane over a 1.6 msec period during the explosion. Three radar systems with 120° spacing measured the velocity of fragments at the axial mid-plane during the last stage of the measurement window. The rapid sampling of the strain gauges, PDV probes, and radar signals was triggered by break wires running the length of the vessel from the upper outside flange to the lower outside flange. In order to capture data prior to the wire break, the data was looped through the oscilloscopes.

Experimental results

The violence recorded in the STEX deflagration test was moderately high. The explosion removed supports holding the top Lexan panel in place. The end flanges and bolts were significantly deformed (Figure 2). A high speed video footage of the test showed a bright region in the lower cap area, a clear indication of the potential partial loss of confinement during ignition and pressurization. An inspection of the end caps indicated a possibility of a friction weld failure between the tube and flanges, in addition to a, more common, seal leak between the end cap and flange.

Figure 2. The experimental setup after the explosion.

We managed to recover 157 AerMet 100 fragments with a total mass comprising 77.6 % of the tube mass. The fragment mass distribution is shown in the histogram of Figure 3. The median fragment mass was 1.1 g and a typical fragment had the size of 2 cm. Based on the average final thickness of the fragments, the real strain at fracture was approximately 15% (14% engineering strain).

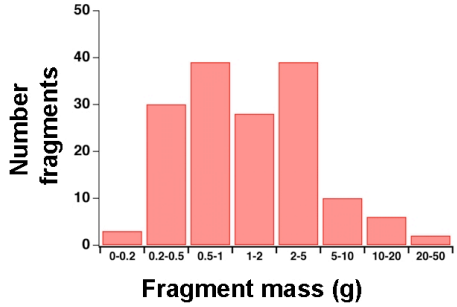

Figure 3. Fragment mass distribution.

The tube wall velocity measurements from the three PDV probes and radar systems are plotted versus time relative to the trigger point in Figure 4. The PDV measurements span nearly four orders of magnitude. For velocities less than 1 m/s, there are significant differences between the results for the three PDV probes, suggesting some asymmetry in the early expansion. There is also more uncertainty in the measurements at these low velocities as evidenced by the increased measurement noise as the limits of the sensor are approached. We believe the dip in velocities at around –130 μs is the result of a leak in the lower end cap area. A high speed video image at t=–100 μs showed a bright region in the lower end cap area. An inspection of the end caps seemed to suggest the possibility of failures of the friction welds between the tube and end flanges, but post-test analysis adds the possibility of an O-ring failure between the end cap and flange. Analysis is still in progress. At the larger velocities, the three probes deliver very similar results, indicating remarkable symmetry in the expansion of the tube. The maximum measured PDV velocity is 720 m/s as given by probe no. 2. The three radar systems gave velocities the following velocities: Radar 1-2140, 1250 m/s, Radar 2-2100, 650, 70 m/s and Radar 3-960, 1150 and 930 m/s. The mean value of all radar velocities was 1070 m/s. The radar measurements continue the curve formed by the three PDV probes. The explosion occurs on the scale of 200 μs, indicating a deflagration.

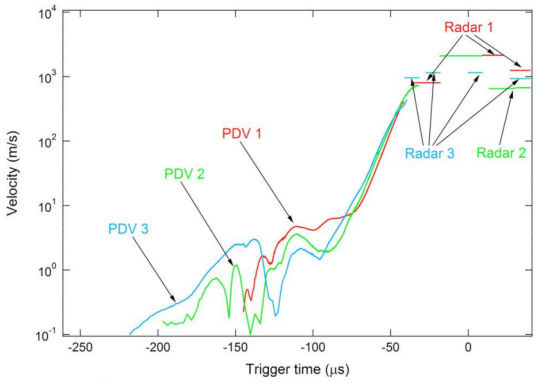

Figure 4. Tube wall velocity based on PDV probes and radar.

PDV and radar results for the radial displacements of the tube wall and fragments are

plotted versus time in Figure 5. The PDV curves were obtained by integrating the velocity curves of Figure 4 using the initial position from SG1. The PDV curves were extended using the average radar velocity and the final wall position calculated from PDV2. The results from the two strain gauges, three PDV probes, and three radar systems provide a single curve for 10 cm of wall motion, corresponding approximately to a 400% radial expansion. At the fracture limit of 14%, the PDV velocity is approximately 390 m/s. Since velocities increase to 1070 m/s, there appears to be considerable acceleration after fracture. These results suggest that both measurements and models need to include behavior after fragmentation to characterize violence.

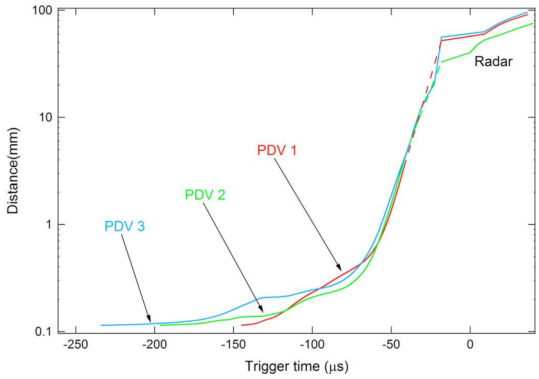

Figure 5. Tube wall position based on PDV probes and radar.

ALE3D MODELLING OF STEX IGNITION/DEFLAGRATION TEST

Our over-arching goal is the development of a multi-physics computer (ALE3D) model capable of accurately describing the pure deflagration test in three-dimensions. We envision the model being systematically validated against available experimental data using a set of clearly defined metrics (e.g. fragment velocity, fragment size distribution, etc.), and, eventually, allowing to carry out fully predictive simulations. Undoubtedly, this is a very ambitious but also extremely challenging, objective. The challenges may include: the development of accurate deflagration models, a model of the thermo-mechanical response of the vessel under extreme pressures and temperatures, a description of strain-localization and fracture, handling of the HE leakage through the gaps in the expanding vessel, etc. Whereas the STEX test is inherently three-dimensional, valuable insight can be gained from simpler two-dimensional models. In this section, we present numerical results of our ALE3D simulations of the deflagration test in a two-dimensional configuration.

ALE3D LX-10 material model

We have developed an ALE3D chemical, mechanical, and thermal model of the LX-10. We use a burn front model in which solid HMX and Viton reactants are converted to gaseous products in a single reaction step. We assume that the burn front velocity, V, is a function of the pressure, P, at the front location, and use power-law expressions of the form to describe segments of the burn front curve:

$$V = V_0 (P/P_0)^n \qquad (1)$$

Here the subscript 0 indicates a reference quantity.

The mechanical response of the solid HMX, along with the Viton reactant, is represented by the Steinberg-Guinan model with a 7-term polynomial equation of state (EOS) [5]. The solid constituents are taken to be perfectly plastic above the yield point (no strain-hardening).

The expression for the EOS of the unreacted explosive follows a seven-term polynomial in the form of

$$P(\xi,T)=a_0+a_1\,\xi + a_2\,\xi^2 + a_3\,\xi^3 + (b_0 + b_1\,\xi + b_2\,\xi^2)\,\rho_0\,c_v\,(T-T_0), \qquad (2)$$

where: P is the pressure, $\xi=\rho/\rho_0 - 1$ denotes the volumetric compression, ρ_0 – the reference density, ρ-density, c_v-constant volume heat capacity, T-temperature and T_0-reference temperature. The heat capacity is assumed independent of temperature. a_0, a_1, a_2, a_3 and b_0, b_1, b_2 are constant parameters. We set $a_0=b_2=0$ and $b_0=b_1$. The remaining parameters are adjusted by means of non-linear regression to provide the best fit of thermal expansion, heat capacity, temperature-dependent hydrostatic compression, and the unreacted shock Hugoniot (c.f. [3]). Calculated melt and cold curves are used to account for the influence of compression on melting energy.

The model gas constituents are treated as no-strength materials with gamma-law equations of state

$$P=(\gamma\text{-}1)\,\rho_0\,c_v\,T \qquad (3)$$

Here, P is the pressure, and γ is a constant parameter. This type of EOS provides a representation over much of the pressure range, except at the higher pressures of 10 kbar (1 GPa) where the model may be less accurate. The value of γ for the HE gas species is set using pressure of 1 kbar (100 MPa), temperature of 2273°K, and the density and heat capacity from the thermo-chemical equilibrium computer code, CHEETAH 3.0 [4] for the final product gases.

For all solid LX-10 constituents, the shear modulus, μ, the yield stress, Y, are assumed to vary with temperature, but remain strain-rate independent. In addition, μ an Y decrease to zero upon melting.

The time-dependent thermal transport model includes the effects of conduction, reaction, advection, and compression. The constant-volume heat capacity is constant for each reactant consistent with the Steinberg-Guinan model. The thermal conductivity for the condensed species is taken to be constant, whereas the effects of temperature are included for the gaseous species. The heat capacity for the final gaseous products gases is assigned the same constant-volume value used in the gamma-law model. The temperature-dependent thermal conductivity is estimated at 1 kbar (100 MPa) using Bridgman's [6] equation for liquids in which the sound velocity is calculated using results from CHEETAH 3.0 [4].

The material parameters for the above models were assembled from measurements obtained for LX-10 samples investigated in earlier studies [7].

The deflagration rate of LX-10 was measured with the LLNL High Pressure Strand Burner [9]. This system measures pressure during the burn and also the progress of the burn front with wires that melt as the flame advances. Cylindrical samples 6.4 mm diameter x 5.7 cm long are prepared by stacking nine pieces to form a burn tower. Temporal pressure data along with time of arrival data at each burn wire provide the information to calculate burn rate as a function of pressure.

The deflagration rate measurements are plotted versus pressure in Figure 6 for samples burned at room temperature. It is seen that the burn rates are high and have considerable scatter. Below approximately 100 MPa the measurements seem to follow a single curve, suggesting a smooth laminar burn. Also shown are measurements for LX-04 which follow the data for LX-10 very closely. At higher pressures many of the LX-10 data points are larger by as much as three orders of magnitude than the values on the laminar burn curve for LX-04 (85% HMX, 15% Viton A). We believe that the samples of LX-10 are deconsolidating at higher pressures which leads to increased surface area and a much higher effective burn rate. It seems that the increased binder in LX-04 is retarding the deconsolidation as the measurements follow single straight line. The LX-10 burn rate measurements are represented by one power-law burn rate model (see Eq. (1)) with n=1 in the laminar burn region below approximately 200 MPa. It is an open question as to how to represent the behavior of LX-10 in the deconsolidation region. We use a second power-law model with a steeper slope of n=6.4 which passes through the middle of the measurements in the deconsolidation region.

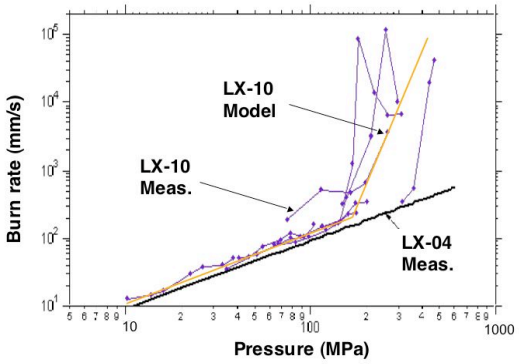

Figure 6. Power-law model for burn rates for LX-10.

ALE3D AerMet 100 material model

The mechanical response of the AerMet 100 tube was assumed to follow the Steinberg-Guinan model [5] with the Gruneisen EOS. The strain hardening was incorporated through power-law relation between the yield stress, Y, on the equivalent plastic strain, $\bar{\varepsilon}^p$,:

$$Y = Y_0\left[1+\beta(\bar{\varepsilon}^p+\bar{\varepsilon}_0^p)\right]^n\frac{\mu}{\mu_0}. \qquad (4)$$

Here, Y_0, $\bar{\varepsilon}^p$ and μ_0 denote, respectively, the reference state values of the yield stress, equivalent plastic strain and the shear modulus. μ is the shear modulus and β a parameter. Following Steinberg *et al*. [5] we assumed that the shear stress, μ, changed according to

$$\mu = \mu_0 \left[1 + b\frac{P}{\eta^{1/3}} - h(T - T_0) \right], \quad (5)$$

where: b and h are material parameters. In the above expressions, we have:

$$\eta = \frac{\rho}{\rho_0},$$

$$\bar{\varepsilon}^p = \int \dot{\bar{\varepsilon}}^p dt,$$

$$\dot{\bar{\varepsilon}}^p = \sqrt{\frac{2}{3}\left[(\dot{\varepsilon}_1^p - \dot{\varepsilon}_2^p)^2 + (\dot{\varepsilon}_2^p - \dot{\varepsilon}_3^p)^2 + (\dot{\varepsilon}_3^p - \dot{\varepsilon}_1^p)^2 \right]}.$$

The principal values of the plastic strain rate are denoted as $\dot{\bar{\varepsilon}}_i^p$. The reference state corresponds to $T_0 = 300$ K, $P_0 = 0$ and $\varepsilon = 0$. In addition, $\bar{\varepsilon}_0^p = 0$ is taken.

The AerMet 100 was allowed to undergo fracture by recourse to the Johnson and Cook [10] failure model. According to this model, a solid loses ability to carry loads when the equivalent plastic strain, $\bar{\varepsilon}^p$, reaches a critical value ε^f. An empirical rule for ε^f has been proposed by Hancock and McKenzie [11]. According to this rule, ε^f is given by the following expression:

$$\varepsilon^f = D_1 + D_2 \exp[D_3(-P/\bar{\sigma})], \quad (6)$$

where: D_1, D_2, and D_3 are materials parameters, $\bar{\sigma}$ is the Mises equivalent stress, and P is the pressure. The failure strains, ε^f, attempt to capture the process of formation, growth and coalescence of voids that emerge from inclusions, defects or impurities. The size of these voids is strongly dependent on the magnitude of stress. As the stress increases the voids tend to coalesce and form cracks. These cracks, in turn, link up and lead to the formation of fragments. In the context of ALE3D, we assumed that the failure strains were distributed over the entire AerMet 100 computational domain in accordance with a Gaussian distribution. To this end, a Gaussian distribution with mean of 10% and standard deviation of 2% for the parameter D_1 in Eq. (6) was adopted. Moreover, each finite element in the mesh had an individual failure strain assigned on the basis of this distribution. If, in the course of the simulation, the strain within an element achieved this critical failure strain, the element would lose its ability to support the load and become a part of a new crack. Subsequently, these "failed" elements merged to form fragments.

The values of the material parameters, as well as fracture data, for AerMet 100 were taken from the work of Couch *et al*. [12].

Details of the ALE3D model

The ultimate objective of our work has been the development of simulation capability that would permit us to routinely model experiments such as the pure deflagration STEX. These computer models should allow reproducing the available experimental data, but also possessing a certain level of predictive ability. However, from a simulation standpoint, modeling of such tests is riddled with challenges. Not only do these models are multi-physics in nature, span largely disparate length and temporal scales, but may also involve dynamic material failure, phase transitions or transport. Effective strategies for building such models are most efficiently developed first in two dimensions and subsequently in three dimensions. To this end, we decided to model a thin axial section of the original vessel assuming periodic boundary conditions along its axis. This approach reduces the three-dimensional nature of the problem and turns it into essentially a two-dimensional one. However, the reduced model still allows gaining substantial insight into the initial stages (until the failure of the vessel) of the STEX experiment. Moreover, in the spirit of reducing the computational cost we chose to model only a quarter of the experimental configuration. It should be noted, however, that this approach is likely to provide an accurate representation of the entire domain.

The STEX experiment, especially following the vessel failure, involves the gaseous reaction products, as well as un-reacted explosive, leaking through incipient cracks into the surrounding environment. In order to model this phenomenon with sufficient accuracy, we assumed that the tube was immersed in air. The air behavior followed the

gamma-law EOS (8), with material parameters from Yoh *et al*. [13].

We tailored the finite element discretization of the computational domain to the problem. Thus, fine mesh regions were located directly in the vicinity of the tube and the mesh remained relatively coarse otherwise. The mesh encompassed the total of 35,968 elements.

A purely Eulerian framework was adopted in order to bypass potential numerical issues related to mesh entanglement, tuning of advection parameters, or adaptive mesh refinement.

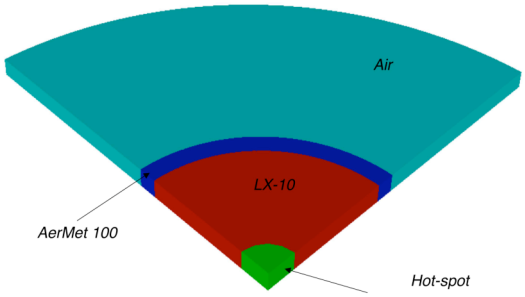

Figure 7. Details of the computational domain for the deflagration of LX-10 confined in an AerMet 100 tube.

The LX-10 ignition was modeled via an artificial hot-spot introduced at the center of the tube (Figure 7). At the onset of the simulation, the temperature of the hot-spot was raised instantly to 700 ^{o}K, which triggered the deflagration reaction.

SIMULATION RESULTS

After the explosive is ignited at time t=0, the burn front begins advancing outward. The resulting high pressure product gases expand the vessel in the radial direction. The time evolution of the burn front position is shown in Figure 8. The snapshots correspond to time t=10, 20, 30, 40, 50 and 55.6 μs. The color-coding represents materials: red-the un-reacted LX-10, green-gaseous reaction products, dark blue-AerMet, and light blue-air. Initially, the burn front emanating from the hot-spot is able to maintain a cylindrical character. However, as the simulation progresses, the burn-front begins to gradually deviate from its original profile, with perturbations appearing along its extent. The emergence of these perturbations seems to be well correlated with the onset of the tube failure and initiation of radial fracture.

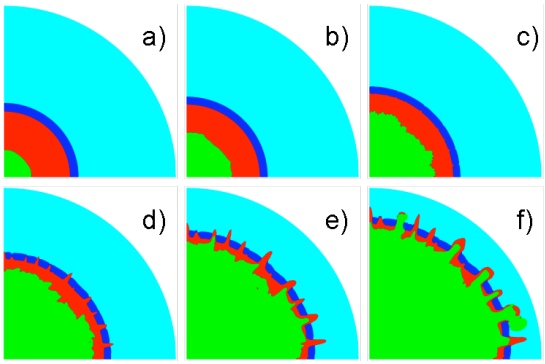

Figure 8. ALE3D simulation of LX-10 deflagration. The six configurations correspond to a) 10 μs, b) 20 μs, c) 30 μs, d) 40 μs, e) 50 μs and f) 55.6 μs.

At approximately 30 μs after the ignition, profound plastic deformation of the tube becomes clearly visible, with cusp-like features forming along its circumference. Moreover, the plastic deformation appears to localize along well defined radial bands. Subsequently, these shear-band structures serve as convenient locations for the initiation and growth of cracks. Once cracks are initiated, they rapidly extend in the radial direction and cross the width of the vessel wall, resulting ultimately in fragmentation of the tube.

The development of cracks in the tube allows for the remaining un-reacted explosive to flow out of the vessel under the pressure of the product gases. This phenomenon is clearly noticeable already at 40 μs, and becomes more pronounced at later times. Additionally, the product gases are at this point allowed to flow around the fragments into the surrounding air. Moreover, the burn of the ejected LX-10 continues outside of the tube.

The final configuration in Figure 8 corresponds to 56.6 μs. This is the last configuration we were able to reach before the stable time step in the calculation became prohibitively small. At this time, the vessel has fragmented entirely, and both the un-reacted LX-10, as well as, the gaseous reaction products are being ejected through rapidly growing gaps between fragments. There is some residual amount of explosive remaining, but the majority has burnt.

Motion of the outside wall of the tube during the STEX test is often considered as a measure of violence in cookoff of energetic materials. Obviously, the coupled thermal-chemical-mechanical behavior of an explosive plays a dominant role in determining the rate of expansion of the vessel. However, this rate is mediated to some extent by the thermo-mechanical response of the vessel itself. In particular, the onset of material failure and subsequent transition to fragmentation is likely to influence the motion of the outside wall. We attempted to identify the failure mechanisms in the tube leading to the initiation and growth of cracks. To this end, we followed the evolution of the equivalent plastic strain, $\bar{\varepsilon}^p$, an internal variable in the Steinberg-Guinan AerMet model. The magnitude of $\bar{\varepsilon}^p$ allows to identify regions of substantial plastic deformation, that subsequently may serve as nucleation sites for shear-band localization. We plot the evolution of the equivalent plastic strain for the STEX vessel in Figure 9. The color coding represents the magnitude of $\bar{\varepsilon}^p$. The four configurations of the tube correspond to a) 22 μs, b) 23 μs, c) 28 μs and d) 33 μs.

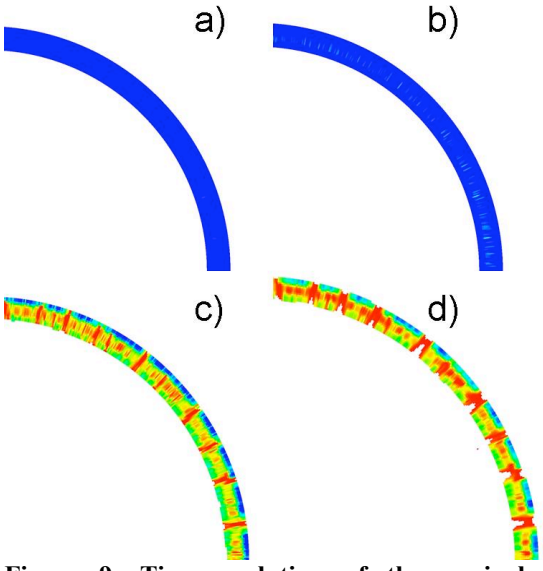

Figure 9. Time evolution of the equivalent plastic strain in the vessel. The color coding represents the magnitude of the plastic strain. The four configurations of the tube correspond to a) 22 μs, b) 23 μs, c) 28 μs, and d) 33 μs.

The initial deformation of the tube is ostensibly elastic, with marginal irreversible (plastic) deformation present. Moreover, the plastic strain remains uniformly distributed along the circumference. The initial signs of strain-localization appear at 23 μs, as radial bands of higher plastic strain emerge. As the deformation of the tube continues, the presence of these bands becomes more evident. Subsequently, these shear-bands serve as convenient sites for the initiation of radial cracks, as is evident in Figure 9 d). Once initiated, these cracks extend in the radial direction and ultimately cross the wall of the tube, resulting in its fragmentation. Obviously, due to imposed two-dimensional character of the overall deformation, the cracks do not display a three-dimensional character.

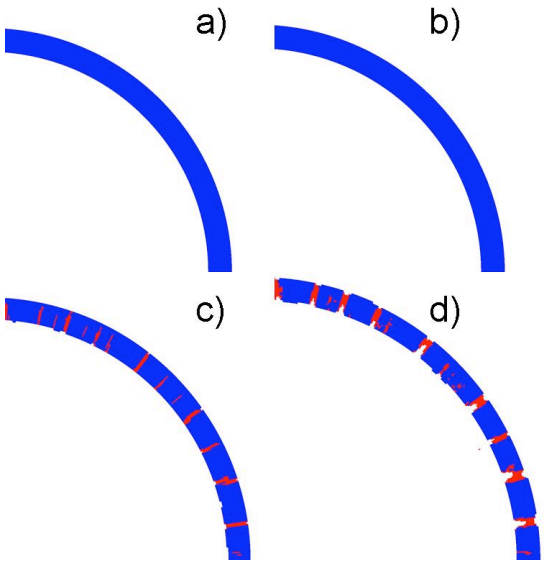

Figure 10. Time evolution of the damage parameter in the vessel. Red indicates material failure, and blue otherwise. The four configurations correspond to a) 22 μs, b) 23 μs, c) 28 μs, and d) 33 μs.

Additional insight into material failure mechanisms leading from strain-localization to crack formation may be obtained with the help of failure strains, ε^f, of the Johnson-Cook failure model. However, instead of using ε^f directly we define the damage parameter, d, to be equal to 0 if ε^f have been reached, or 1 otherwise. We plot the time evolution of d in Figure 10. In contrast with

the evolution of the equivalent plastic strain, the strength of AerMet remains intact until 28 μs, when the indications of fracture in early stages may be observed. The locations of these incipient cracks are well correlated with regions of the tube that have undergone severe plastic deformation.

It is evident now that the cracks initiate at the internal tube surface and gradually propagate through the wall thickness. On the basis of the time evolution of the damage parameter, we can estimate the onset of vessel failure to occur approximately at 28 μs, or 22 % radial strain. The simulated radial strain at failure is therefore considerably higher then the experimental value of 14%. This significant discrepancy between the experiment and simulation is most likely caused by an inadequate description of the fracture processes in the vessel material and requires further studies.

One of the most critical experimental metrics in the investigation of cookoff violence is the time evolution of the velocity and position (displacements) of the outer vessel wall. At this time, our numerical model is only a rudimentary representation of the STEX test; most noticeable is the absence of the three-dimensional character of the experiment from the model. It is, however, informative to extract the two fundamental metrics from simulation results and weigh them against their experimental counterparts.

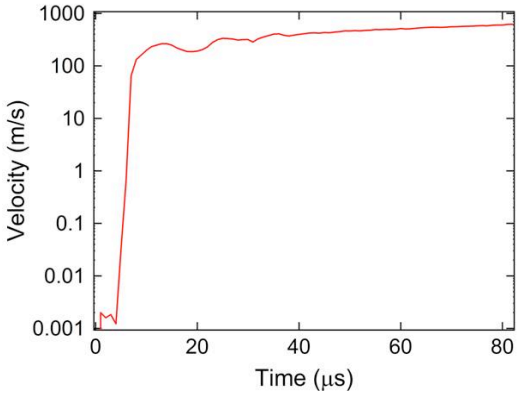

Figure 11. Simulated velocity of the outer tube wall.

The simulated velocity of the outer surface of the tube at 45-degrees from the horizontal axis is plotted in Figure 11. The simulation has been able to capture the character of the experiment reasonably well: the rapid rise followed by a relative plateau. There are, however, substantial quantitative differences. First, the calculation predicts the velocity to increase very quickly, on the order of a few microseconds. The experimental data indicates this rise time to be on the order of 50 microseconds. Second, the terminal velocity in the simulation is 620 m/s (at 82 μs after ignition), whereas the average radar value recorded in the experiment is 1070 m/s.

The onset of the failure of the tube, which occurs at 28 μs, appears uncorrelated with the rapid rise of the velocity taking place before 10 μs. Therefore, during the entire rise the tube deforms plastically, but without significant damage.

The wall tube velocity profile may be integrated in time to yield the time evolution of wall position. We plot the wall position vs. time in Figure 12. There are two distinct regimes in the experimental profile: i) rapid rise, and ii) relative plateau, matching the nature of the velocity profile. The simulated position curve is distinctly different: the two regimes are entirely absent, with the curve simply rising monotonically.

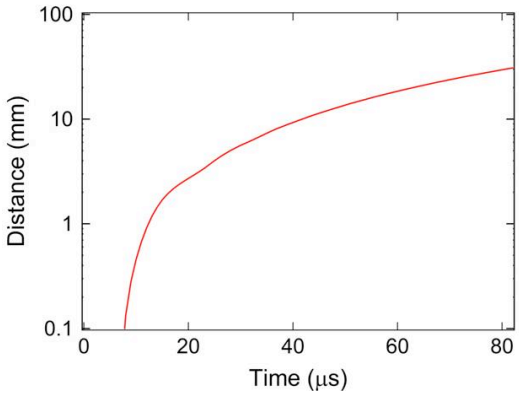

Figure 12. Simulated time evolution of outside tube wall position.

There are many possible reasons for substantial discrepancies between the numerical predictions and the experimental results for the time history of the tube wall velocity and its position. So far, we have not been able to identify the sources of these discrepancies. However, we believe that three sources may dominate: i) inaccurate deflagration rates in LX-10 model, ii) incorrect description of the AerMet mechanical response at strain rates commensurate with the experimental conditions., and iii) the imposed two-dimensional mode of the

deformation. Additional sources of errors may include a simple model of the igniter by means of the hot-spot or LX-10 ignition properties.

Despite the obvious shortcomings in accurately predicting time evolution of tube wall velocity and its position, the simulation is capable of capturing, albeit approximately, magnitudes of both quantities.

SUMMARY AND CONCLUSIONS

We presented the results of an experimental and numerical study of the STEX deflagration test for LX-10. ALE3D models were employed to represent the coupled thermal, chemical and mechanical behavior during the ignition and explosion. Model parameters were obtained from directly from measurements at conditions relevant to the explosive phase of cookoff.

Results of two-dimensional ALE3D simulations of the STEX deflagration test were contrasted with the experimental data by means of well established metrics. The numerical model was shown of being capable of capturing all the essential components of the deflagration phenomenon. However, the model underestimated the cookoff violence recorded in the experiment.

REFERENCES

1. J. L. Maienschein and J. F. Wardell, "The Scaled Thermal Explosion Experiment," *in Proceedings of 12th International Detonation Symposium*, San Diego, CA, 2002.
2. C. M. Tarver and T. D. Tran, " Thermal decomposition models for HMX-based plastic bonded explosives " *Combustion and Flame* (2004) 50-62.
3. M. A. McClelland, J. L. Maienschein and A. L. Nichols, *Joint DoD/DOE Munitions Technology Development Program FY-01 Progress Report, Ignition and Initiation Phenomena: Cookoff Violence Prediction*, Lawrence Livermore National Laboratory, (2002).
4. L. E. Fried, W. M. Howard, *Cheetah 3.0 User's Manual*, Lawrence Livermore National Laboratory, (2001).
5. D. J. Steinberg, S. G. Cochran and M. W. Guinan, J. Appl. Phys, **51**, 1498 (1980)
6. R. B. Bird, W. E. Stewart and E. N. Lightfoot, *Transport Phenomena* (Wiley, 1960) 260-261.
7. T. D. Tran, *A Compilation of One-Dimensional, Time-to-Explosion (ODTX) Test Data for High Explosives and Propellants*, Lawrence Livermore National Laboratory, (2003)
8. E. Catalano, R. McGuire, E. L. Lee, E. Wrenn, D. Ornellas and J. Walton, "The Thermal Decomposition and Reaction of Confined Explosives," *in Proceedings of Sixth International Symposium on Detonation*, Coronado, CA, Office of Naval Research (1976) 214-222.
9. J. L. Maienschein and J. B. Chandler, "Burn Rates of Pristine and Degraded Explosives at Elevated Pressures and Temperatures," *in Proceedings of 11th International Detonation Symposium*, Snowmass, CO, Office of Naval Research (1998).
10. G. R. Johnson and W. H. Cook, Engng Fracture Mech., **21**, 31 (1985).
11. J. W. Hancock and A. C. McKenzie, J. Mech. Phys. Sol., **24**, 147 (1976).
12. R. Couch, D. Nikkel, R. C. Becker, T. Dunn, D. M. Goto, H. K. Springer, D. Lassila and K. Whittaker, *Joint DoD/DOE Munitions Technology Development Program FY-02 Progress Report, 3D Computations and Experiments*, UCRL-ID-103482-02 (2003).
13. J. J. Yoh, M. A. McClelland, J. L. Maienschein, J. F. Wardell and C. M. Tarver, J. Appl. Phys., 97, 083504 (2005).

This work was performed under the auspices of the U. S. Department of Energy by University of California, Lawrence Livermore National Laboratory under contract W-7405-Eng-48.